Geophysical Research Letters

CONTINUED Supporting Information for

Pitted Terrains on (1) Ceres and Implications for Shallow Subsurface Volatile Distribution

H. G. Sizemore*[1], T. Platz[2], N. Schorghofer[1], T. H. Prettyman[1], M. C. De Sanctis[4], D. A. Crown[1], N. Schmedemann[5], A. Neesemann[5], T. Kneissl[5], S. Marchi[6], P. M. Schenk[7], M. T. Bland[8], B. E. Schmidt[9], K. H. G. Hughson[10], F. Tosi[4], F. Zambon[4], S. C. Mest[1], R. A. Yingst[1], D. A. Williams[11], C. T. Russell[10], C. A. Raymond[12]

[1]Planetary Science Institute, Tucson AZ, USA,
[2]Max Planck Institute for Solar System Research, Göttingen, Germany,
[4]Istituto di Astrofisica e Planetologia Spaziali, INAF, Rome, Italy,
[5]Freie Universität Berlin, Berlin, Germany,
[6]Southwest Research Institute, Boulder, CO, USA,
[7]Lunar and Planetary Institute, Houston, TX, USA,
[8]USGS Astrogeology Science Center, Flagstaff, AZ, USA
[19]Georgia Institute of Technology, Atlanta, GA, USA,
[10]University of California Los Angeles, Los Angeles, CA, USA,
[11]Arizona State University, Tempe, AZ, USA,
[12]Jet Propulsion Laboratory, California Institute of Technology, Pasadena, CA, USA.

Contents of this file (part 2)	**Contents of previous file (part 1)**
Figures S6 to S12	Text S1 to S12 Figures S1 to S5 Table S1

Introduction

The supplementary materials include context and detailed images of cerean all cerean craters in which pits have been identified (S1-7), as well as technical background for pit size measurements (S8), sublimation (S9) and outgassing (S11) calculations, comparisons to extra-cerean morphological features (S10), and a description of thermal image analysis (S12).

Annex 6

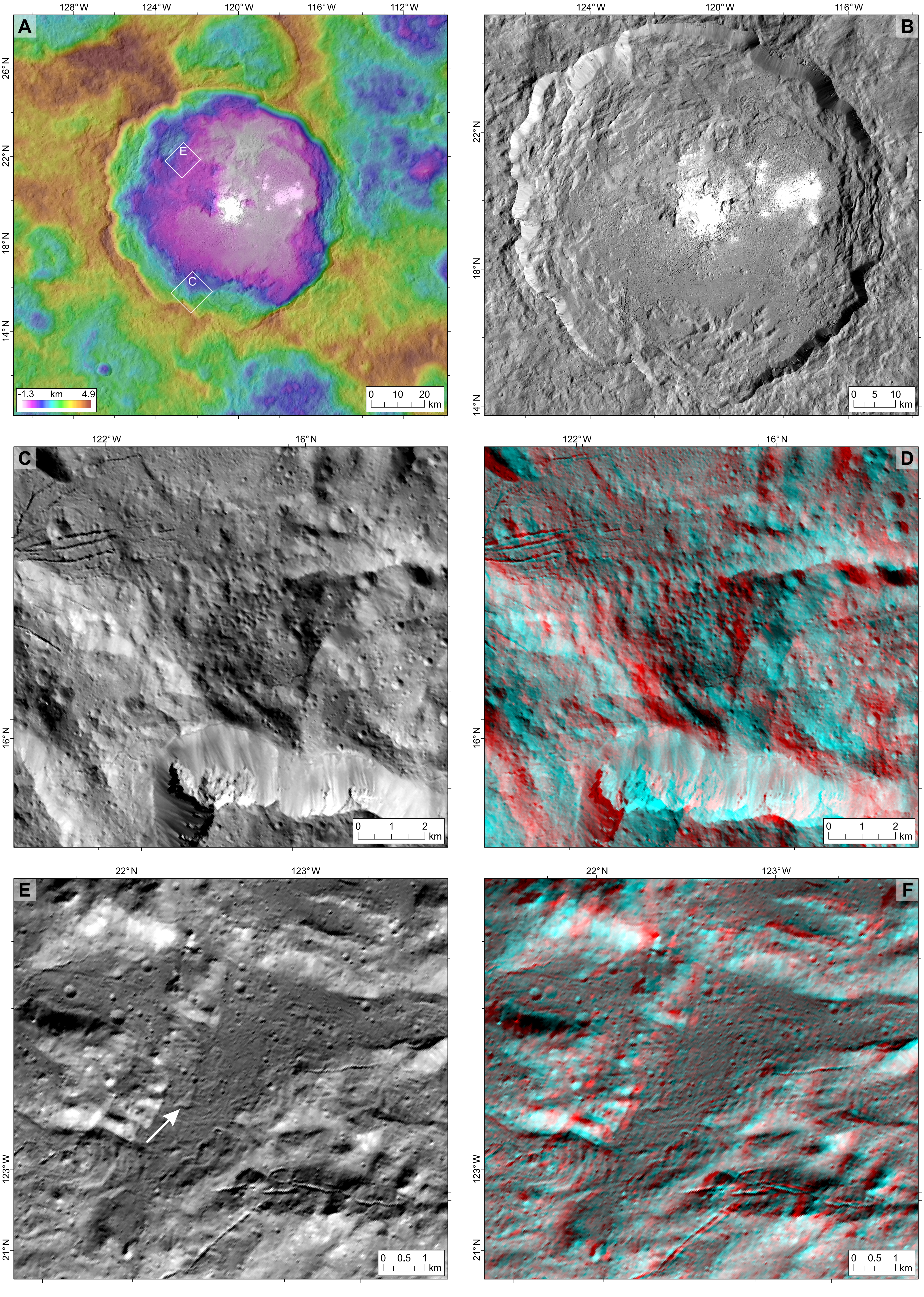
A
128° W
124° W
120° W
116° W
112° W
26° N
22° N
18° N
14° N
E
C
-1.3 km 4.9
0 10 20 km
B
124° W
120° W
116° W
22° N
18° N
14° N
0 5 10 km
C
122° W
16° N
16° N
0 1 2 km
D
122° W
16° N
16° N
0 1 2 km
E
22° N
123° W
123° W
21° N
0 0.5 1 km
F
22° N
123° W
123° W
21° N
0 0.5 1 km

Fig. S6: Occator Crater (D=92 km, 19.82°N/239.33°E).

(A) Overview of the surrounding terrain of Occator with superimposed HAMO stereophotogrammetry-based digital elevation model (≈137 m/px); colour-coded heights are given relative to the reference ellipsoid 482 km × 482 km × 446 km (Preusker et al., 2016). White boxes show the locations displayed in panels **C**-**F**. (**B**) Occator in panchromatic imagery. Cerealia Facula is located within the central pit; Vinalia Faculae are located on a large wall collapse-sourced lobate deposit (Nathues et al., 2017). (**C**) Pitted terrain southwest of the central pit developed within terrace materials. (**D**) 3D anaglyph of panel **C** based on Framing Camera images 59,294 and 75,000. (**E**) Lobate terrace material. Note atypical elongated depression indicated by white arrow was not included in "pit" analysis. (**F**) 3D anaglyph of panel E based on Framing Camera images. All scenes except **D** and **F** are excerpts of the Framing Camera panchromatic nadir mosaic (30 m/px; equidistant cylindrical projection centred at 19.5°N/239.5°E). Note north is <u>not</u> up in panels **C-F**.

Annex 7

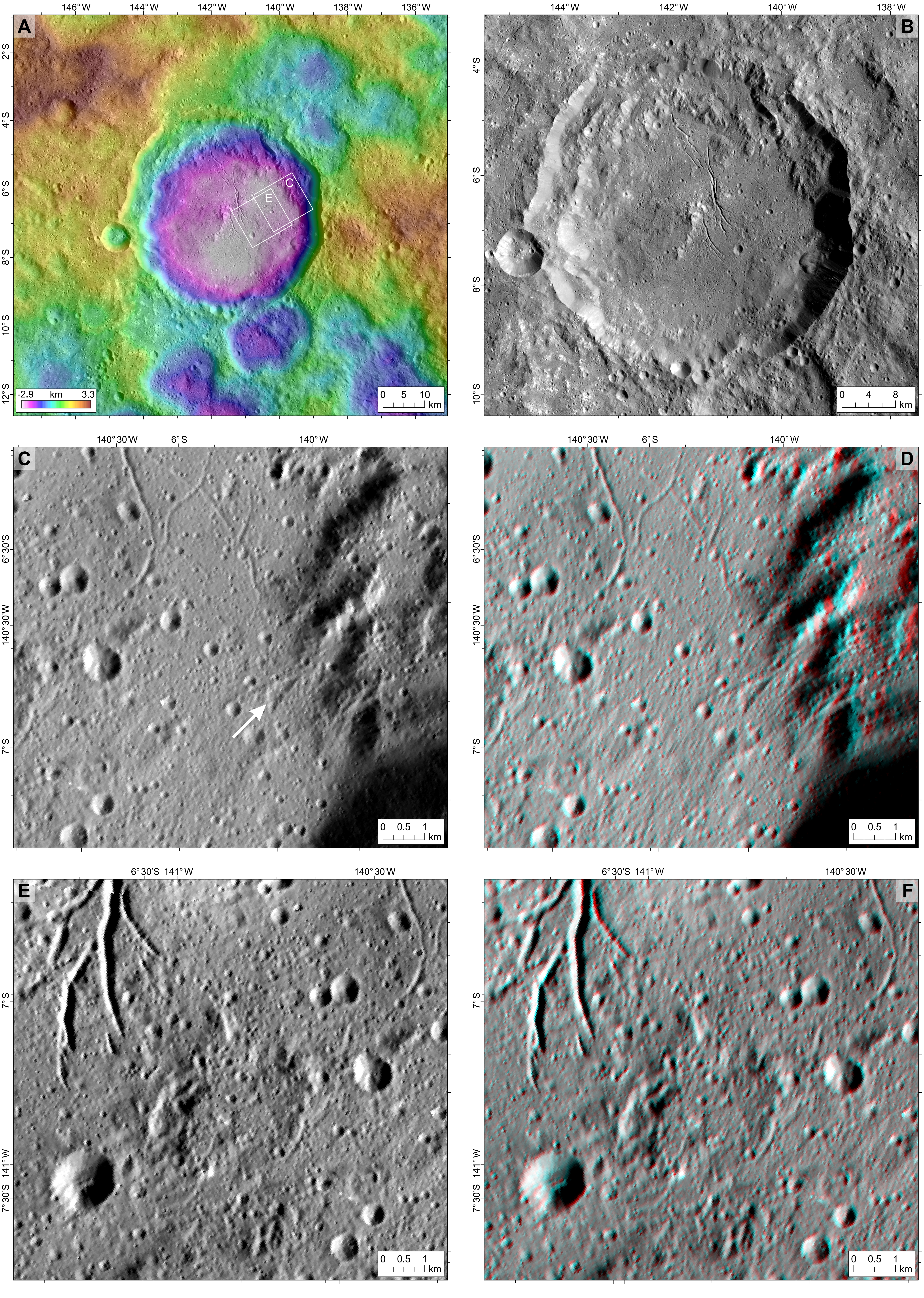
A
146° W
144° W
142° W
140° W
138° W
136° W
2° S
4° S
6° S
8° S
10° S
12° S
C
E
-2.9 km 3.3
0 5 10 km
B
144° W
142° W
140° W
138° W
4° S
6° S
8° S
10° S
0 4 8 km
C
140° 30'W
6° S
140° W
6° 30'S
140° 30'W
7° S
0 0.5 1 km
D
140° 30'W
6° S
140° W
6° 30'S
140° 30'W
7° S
0 0.5 1 km
E
6° 30'S 141° W
140° 30'W
7° S
7° 30'S 141° W
0 0.5 1 km
F
6° 30'S 141° W
140° 30'W
7° S
7° 30'S 141° W
0 0.5 1 km

Fig. S7: Azacca Crater (D=49.9 km, -6.66°N/218.4°E).

(A) Overview of Azacca and its surrounding terrain with superimposed HAMO stereophotogrammetry-based digital elevation model (≈137 m/px); colour-coded heights are given relative to the reference ellipsoid 482 km × 482 km × 446 km (Preusker et al., 2016). White boxes show the locations displayed in panels **C**-**F**. (**B**) Azacca in panchromatic imagery. (**C**) Elongated depression (white arrow) on Azacca floor. (**D**) 3D anaglyph of panel **C** based on Framing Camera images 54,233 and 65,243. (**E**) Potential pitted terrain near a fracture system east of the central peak. (**F**) 3D anaglyph of panel **E** based on Framing Camera images 54,233 and 62,777. All scenes except **D** and **F** are excerpts of the Framing Camera panchromatic nadir mosaic (30 m/px; equidistant cylindrical projection centred at 19.5°N/239.5°E). Note north is not up in panels **C-F**. Note also that Azacca was excluded from pit-size analysis highlighted in Fig. S8 due to the atypical morphology of the depression in panel **C** above and ambiguity between possible pits and craters at other locations on the Azacca floor.

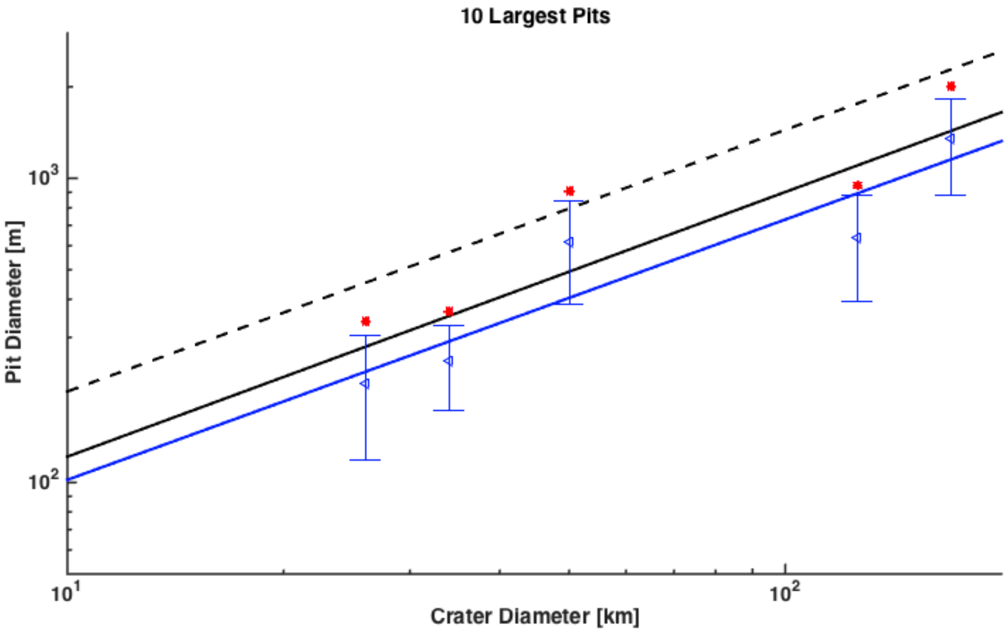

Fig. S8. Pit and Crater Diameter Relationship

Maximum pit diameter (D_{max}) and average diameter of the 10 largest pits (D_{top10}) in the interior of Kupalo, Haulani, Ikapati, Dantu, and Urvara craters as a function of crater diameter. Blue circles represent D_{top10}; error bars are based on statistics of measurements of 10 pits using the ArcGIS CraterTools add-in. Red asterisks represent the diameter of the largest pit as measured using CraterTools. The solid blue line is a power law fit to D_{top10}, $14.2y=x^{0.86}$. Power law fits to data from 13 martian craters by Tornabene et al. [2012] are shown for reference. The dashed black line is maximum pit diameter (D_{max}), $y=27.5x^{0.86}$; solid black line is avg. of 10 largest diameters (D_{top10}), $y=16x^{0.87}$. Note that Azacca and Occator craters were excluded from this analysis, as no pits were identified on the Occator floor and pit identifications at Azacca were ambiguous.

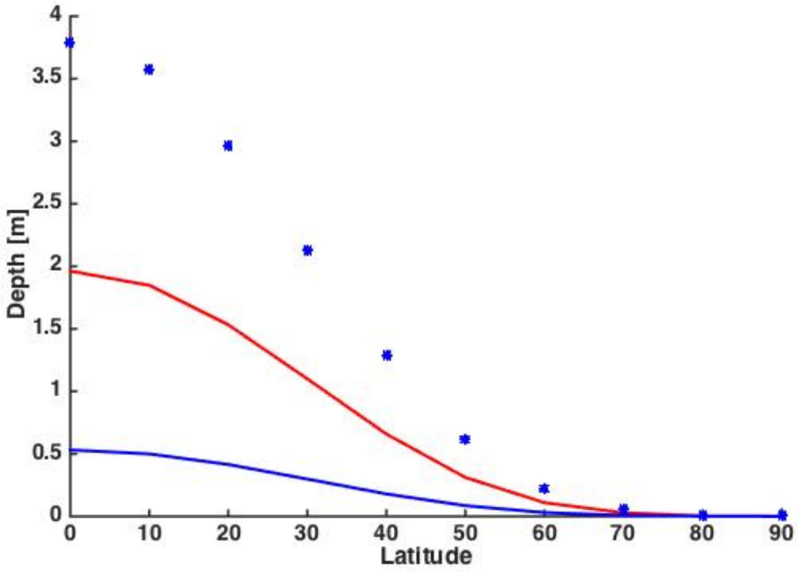

Fig. S9. Maximum pit relief (i.e. depth) due to 1 Ga of sublimation as a function of latitude.

Red line indicates the thickness of the dry silicate lag layer if ice comprises 40 vol.% of near-surface material. Blue line indicates the lag thickness if ice comprises 90 vol.% of near surface material. Blue stars indicate collapse of the surface due to loss of volumetrically dominant ice in the 90 vol.% scenario.

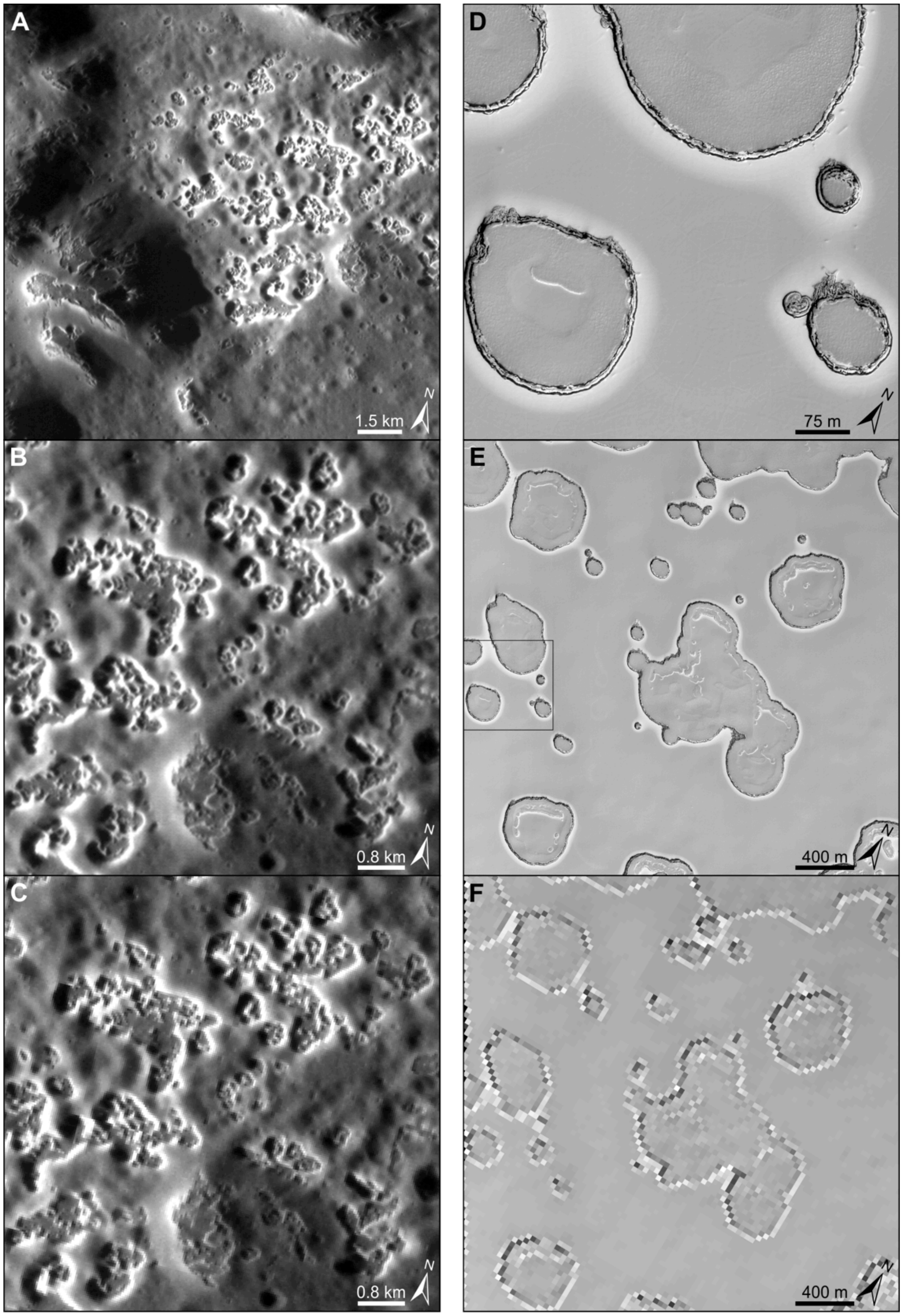
A
1.5 km
N
B
0.8 km
N
C
0.8 km
N
D
75 m
N
E
400 m
N
F
400 m
N

Fig. S10. Mercurian hollows and martian Swiss cheese.

(A) Mercurian hollows with bright halos formed on flat terrain and peak-ring material of Raditladi basin. Hollows appear clustered or are isolated with elongated or branching margins (Mercury Messenger MDIS image EN0220979993M; 17 m/px). (B) Close up of (A). The same scene is shown in (C) downsampled to 35 m/px to match LAMO resolution. (D) Swiss cheese terrain on Mars illustrating near-circular to elliptical depressions with flat floors and complex branching, steep-sided margins. These depressions are associated with the sublimation of a nearly-pure CO_2 layer. The scene is a close-up of (E) (Mars Reconnaissance Orbiter HiRISE image PSP_004989_0945; 0.25 m/px). (F) The same scene as in (E) is shown downsampled to Ceres LAMO resolution (35 m/px).

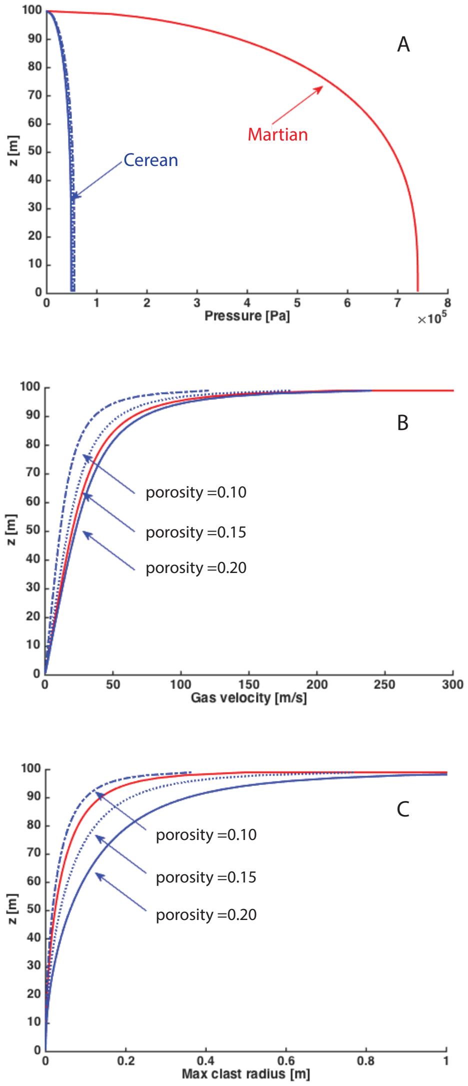A
z [m]
100
90
80
70
60
50
40
30
20
10
0
Pressure [Pa]
0
1
2
3
4
5
6
7
8
×10^5
Martian
Cerean
B
z [m]
Gas velocity [m/s]
0
50
100
150
200
250
300
porosity =0.10
porosity =0.15
porosity =0.20
C
z [m]
Max clast radius [m]
0
0.2
0.4
0.6
0.8
1
porosity =0.10
porosity =0.15
porosity =0.20

Fig. S11. Application of Boyce et al. [2012] Pit Development Model to Ceres

Comparison of (A) pore pressures, (B) gas outflow velocities, and (C) maximum size of elutriated clasts in a 100 m thick layer of volatile-rich crater material. Red lines indicate predictions for Mars (reproduced from Boyce et al. [2012]); blue lines indicate predictions for Ceres.

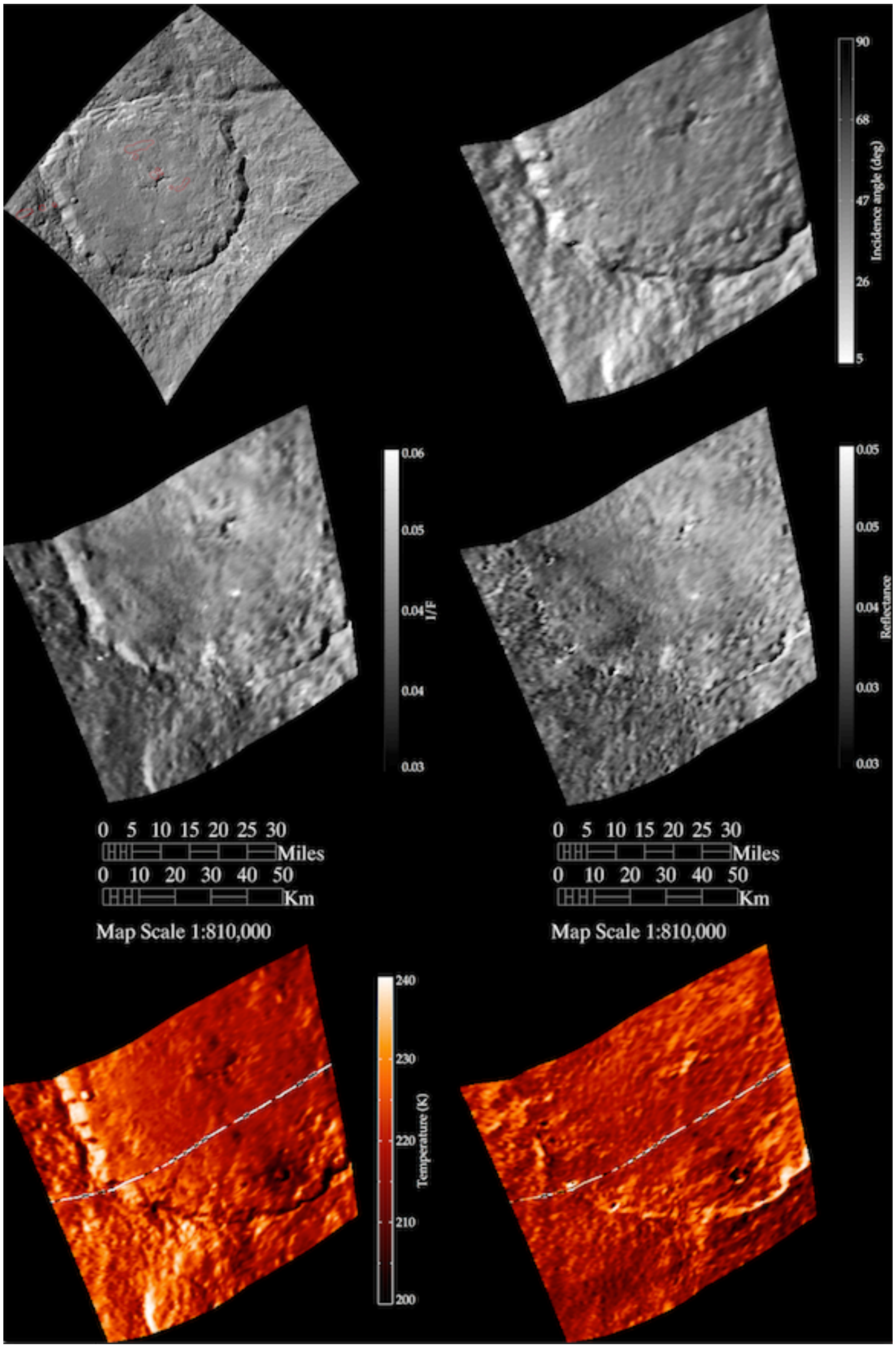
90
68
47
26
5
Incidence angle (deg)
0.06
0.05
0.04
0.04
0.03
I/F
0.05
0.05
0.04
0.03
0.03
Reflectance
0 5 10 15 20 25 30
Miles
0 10 20 30 40 50
Km
Map Scale 1:810,000
0 5 10 15 20 25 30
Miles
0 10 20 30 40 50
Km
Map Scale 1:810,000
240
230
220
210
200
Temperature (K)

Fig. S12. Overview of thermal analysis at Dantu.

(A) Greyscale FC image of Dantu, acquired in the clear filter during HAMO at a spatial resolution of 140 m/px and represented in equirectangular projection with pitted regions outlined in red. VIR data of the same area acquired during the HAMO phase (376 m/px) at a heliocentric distance of 2.958 AU, are displayed in the other panels, also in equirectangular projection. (B) Map of solar incidence angle measured from the surface normal to a detailed shape model of Ceres in the VIR observation. (C) I/F value at the wavelength of 1.2 µm (without photometric correction). (D) Reflectance values at 1.2 µm (photometrically corrected). In panel D, shadows induced by topography are largely smoothed out, and the resulting gray shades are indicative of inherently bright and dark materials. (E) Surface temperature computed from VIR thermal infrared data, as observed at 9.26 ± 0.11 h local solar time. (F) Temperatures in E corrected for the lighting geometry, assuming that the surface of Ceres behaves like a black body (i.e., temperature in panel E divided by the fourth root of the cosine of the solar incidence angle). Regions with intrinsically low (or high) temperature due to distinct thermophysical properties should appear dark (or bright) in both panels E and F. A scale bar accounts for the size of the features observed in the scene.

References:

Becker, K. J., R. W. Gaskell, L. LeCorre, V. Reddy 2015. Hayabusa and Dawn Image Control from Generation of Digital Elevation Models for Mapping and Analysis. *46th Lunar and Planetary Science Conference*, abstract #2955.

Blewett et al. 2011. Hollows on Mercury: MESSENGER Evidence for Geologically Recent Volatile-Related Activity. *Science*, 333, 1856-1859.

Boyce, J. M., L. Wilson, P. J. Mouginis-Mark, C. W. Hamilton, L. L. Tornabene 2012. Origin of small pits in martian impact craters. *Icarus, 221,* 262-275.

Byrne, S. and Ingersoll, A. P. 2003. A Sublimation Model for Martian South Polar Ice Features. *Science*, 299, 1051-1053.

Capria, M. T., F. Tosi, M. C. De Sanctis, F. Capaccioni, E. Ammannito, A. Friegeri, F. Zambon, S. Fonte, E. Palomba, D. Turrini, T. N. Titus, S. E. Schröder, M. Toplis, J.-Y. Li, J.-P. Combe, C. A. Raymond, C. T. Russell 2014. Vesta surface thermal properties map. *Geophys. Res. Let.,* doi: 10.1002/2013GL059026.

Denevi, B. W., D. T. Blewett, D. L. Buczkowski, F. Capaccioni, M. T. Capria, M. C. de Sanctis, W. B. Garry, R. W. Gaskell, L. Le Corre, J.-Y. Li, S. Marchi, T. J. McCoy, A. Nathues, D. P. O'Brien, N. E. Petro, C. M. Pieters, F. Preusker, C. A. Raymond, V. Reddy, C. T. Russell, P. Schenk, J. E. C. Scully, J. M. Sunshine, F. Tosi, D. A. Williams, D. Wyrick 2012. Pitted terrain on Vesta and implications for the presence of volatiles. *Science, 338*, 246-249.

Kneissl, T., S. van Gasselt, G. Neukum 2011. Map-projection-independent crater size-frequency determination in GIS environments – New software tool for ArcGIS. *Planetary and Space Science, 59,* 1243-1254.

Malin, M. C. and K. S. Edget 2001. Mars Global Surveryor Mars Orbiter Camera: Interplanetary cruse through primary mission. *J. Geophys. Res. – Planets, 110,* 23429-23570.

Malin, M. C., Caplinger, M. A., and Davis, S. D. 2001. Observational Evidence for an Active Surface Reservoir of Solid Carbon Dioxide on Mars. *Science*, 294, 2146-2148.

Marchi et al. 2013. High-velocity collisions from the lunar cataclysm recorded in asteroidal meteorites. *Nature Geoscience*, 6, 303-307.

Mouginis-Mark, P. J., and H. Garbiel 2007. Crater geometry and ejecta thickness of the martian impact crater Tooting. *Meteorit. Planet. Scie. 42,* 1615-1625.

Preblich, B., A. McEwen, D. Studer 2007. Mapping rays and secondary craters from Zunil, Mars. *J. Geophys. Res. – Planets, 112,* doi:10.1029/2006JE002817.

Preusker, F., et al. 2016. Dawn at Ceres – Shape Model and Rotational State. *47th Lunar and Planetary Science Conference*, abstract #1954.

Reddy, V., et al. 2012. Color and albedo heterogeneity of Vesta from Dawn. *Science 336,* doi: 10.1126/science.1219088.

Rivkin, A. S. et al. 2010. The Surface Composition of Ceres. *Space Science Reviews 163*, 95-116.

Schorghofer, N. 2008. The lifetime of ice on main belt asteroids. *Ap. J., 682,* 697-705.

Schorghofer, N. 2016. Predictions of depth-to-ice on asteroids based on an asynchronous model of temperature, impact stirring, and ice loss. *Icarus 276*, 88- 95.

Tosi, F., M. T. Capria, M. C. De Sanctis, J.-Ph. Combe, F. Zambon, A. Nathures, S. E. Schröder, J.-Y. Li, E. Palomba, A. Longbardo, D. T. Blewett, B. W. Denevi, E. Palmer, F. Capaccioni, E. Ammanito, T. M. Titus, D. W. Mittlefehldt, J. M. Sunshine, C. T. Russell, C. A. Raymond 2014. Thermal measurements of dark and bright surface features on Vesta as derived from Dawn/VIR. *Icarus, 240,* 36-57.

Tornabene, L. L., et al. 2006. Indentification of large (2-10 km) rayed craters on Mars in THEMIS thermal infrared images: Implications for possible martian meteorite source rgeions. *J. GEophys. Res. – Planets, 111.* Doi:10.1029/2005JE002600.

Tornabene, L. L., et al. 2012. Widespread crater-related pitted materials on Mars: Further evidence for the role of target volatiles during the impact process. *Icarus, 220,* 348-368.